AGU PUBLICATIONS

JGR

Journal of Geophysical Research: Solid Earth

RESEARCH ARTICLE
10.1002/2015JB012768

On the frequency dependence and spatial coherence of *PKP* precursor amplitudes

Nicholas Mancinelli[1], Peter Shearer[1], and Christine Thomas[2]

[1]Scripps Institution of Oceanography, University of California, San Diego, La Jolla, California, USA, [2]Institut für Geophysik, Westfälische Wilhelms Universität Münster, Münster, Germany

Key Points:
- The frequency dependence of PKP precursor amplitudes indicates multiscale lower mantle structure
- Strong lower mantle scattering beneath Central/North America, East Africa, and the West Pacific
- Improvised array in Southern California detects out-of-plane scattering on the receiver side

Correspondence to:
N. Mancinelli,
nicholas_mancinelli@brown.edu

Citation:
Mancinelli, N., P. Shearer, and C. Thomas (2016), On the frequency dependence and spatial coherence of *PKP* precursor amplitudes, *J. Geophys. Res. Solid Earth*, *121*, doi:10.1002/2015JB012768.

Received 22 DEC 2015
Accepted 12 FEB 2016
Accepted article online 15 FEB 2016

Abstract Studies now agree that small-scale (~10 km) weak (~0.1%) velocity perturbations throughout the lowermost mantle generate the globally averaged amplitudes of 1 Hz precursors to the core phase, *PKP*. The possible frequency dependence and spatial coherence of this scattered phase, however, has been given less attention. Using a large global data set of ~150,000 *PKP* precursor recordings, we characterize the frequency dependence of *PKP* precursors at central frequencies ranging from 0.5 to 4 Hz. At greater frequencies, we observe more scattered energy (relative to the reference phase PKP_{df}), particularly at shorter ranges. We model this observation by invoking heterogeneity at length scales from 2 to 30 km. Amplitudes at 0.5 Hz, in particular, suggest the presence of more heterogeneity at scales >8 km than present in previously published models. Using a regional bootstrap approach, we identify large (>20°), spatially coherent regions of anomalously strong scattering beneath the West Pacific, Central/North America, and—to a lesser extent—East Africa. Finally, as proof of concept, we use array processing techniques to locate the origin of scattered energy observed in Southern California by the Anza and Southern California Seismic Networks. The energy appears to come primarily from out-of-plane scattering on the receiver side. We suggest that such improvised arrays can increase global coverage and may reveal whether a majority of precursor energy comes from localized heterogeneity in the lowermost mantle.

1. Introduction

Small-scale structures in Earth's lowermost mantle scatter seismic energy away from direct seismic waves, exciting a precursory wave train to the inner-core phase PKP_{df} [*Cleary and Haddon*, 1972]. Studies now agree that small-scale (~10 km) velocity perturbations of ~0.1% distributed throughout the lower mantle match the globally averaged time and range dependence of the precursor amplitudes at 1 Hz [*Margerin and Nolet*, 2003a; *Mancinelli and Shearer*, 2013], but there is still uncertainty regarding the primary type of heterogeneity responsible for lower mantle scattering [*Waszek et al.*, 2015]. Several ideas have been proposed, including partial melt [*Vidale and Hedlin*, 1998], remnants of fossil slabs [*Cao and Romanowicz*, 2007], dense material related to Large Low-Shear Velocity Provinces [*Frost et al.*, 2013], and small-scale structure associated with Ultralow-Velocity Zones [*Yao and Wen*, 2014]. It is also possible that core-mantle boundary (CMB) topography [*Doornbos*, 1978] contributes to the precursor signal, but the emergent nature of the precursor wave train likely requires the presence of additional small-scale heterogeneity several hundred kilometers above the CMB [*Hedlin et al.*, 1997; *Margerin and Nolet*, 2003a; *Mancinelli and Shearer*, 2013]. In order to gain further insight into which of these is the primary cause of lower mantle scattering, we present a study of the frequency dependence and spatial coherence of *PKP* precursors.

Since it has become generally accepted that *PKP* precursors are scattered waves from the deep mantle, several types of random media have been invoked to model them. *Bataille and Flatté* [1988] approximated the spectrum of inhomogeneities in the lowermost mantle by a power law, solving for the exponent by measuring changes in precursor amplitude with respect to scattering angle. *Cormier* [1995] used Gaussian media with correlation lengths from 20 to 35 km and root-mean-square (RMS) velocity perturbations around 10% to synthesize precursor waveforms that matched a limited set of observed seismograms. Shortly thereafter, *Hedlin et al.* [1997] modeled a global stack of precursor waveforms with exponential random media with a correlation length of 8 km. *Margerin and Nolet* [2003a], likewise, modeled global stacks of 1 Hz waveforms with exponential media but found that the observed range dependence was not well matched. To better

fit the observations, they proposed an alternative model richer in small-scale heterogeneity, noting that the correlation length associated with this model was fundamentally unresolvable due to the limited range of observations. Others [*Hedlin et al.*, 1997; *Mancinelli and Shearer*, 2013], however, found that adjusting the correlation length of an exponential model provided sufficient control in fitting range dependence of the precursor energy. The correlation length of an exponential medium marks the scale at which the heterogeneity power spectrum transitions from white (i.e., constant) at large scales to a function that decays as wave number to the power of −4.

Less attention has been paid to the possible frequency dependence of *PKP* precursors. Although regional studies [*Cormier*, 1999; *Thomas et al.*, 1999, 2009] have explored the frequency content of the scattered energy, global studies [*Hedlin et al.*, 1997; *Margerin and Nolet*, 2003a; *Mancinelli and Shearer*, 2013] have focused on observations in a single-frequency band centered at 1 Hz, because the scattered energy has the highest signal-to-noise ratio at that frequency. In theory, observations of scattered energy at a given frequency are primarily sensitive to structure comparable in size to the seismic wavelength. Observations over a range of frequencies, therefore, ought to provide direct constraints on how heterogeneity power changes with length scale and thus should help discriminate between the various types of random media that have been proposed.

Here we present global stacks of *PKP* precursors filtered in four nonoverlapping bands with central frequencies ranging from 0.5 to 4.0 Hz. We show that the range dependence of the scattered energy changes as a function of frequency. To model this observation, we generate synthetics from several types of random media models, ultimately finding that power law heterogeneity spectra with exponents of −3 and −2.6 produce better fits than exponential models. In other words, we find that heterogeneity is not white up to a corner wave number but continuously decreases with smaller scale lengths over the range ∼30 km to ∼2 km, following a power law in wave number. We then attempt to map possible lateral variations in lower mantle scattering strength by comparing regional stacks of data with the global average. We find large-scale regions of strong scattering beneath the West Pacific, Central/North America, and—to a lesser extent—East Africa. The statistical significance of these observations is confirmed by bootstrap resampling and spatial coherence tests. Lastly, we demonstrate as a proof of concept that groups of nearby stations can be used to estimate the source regions of scattered energy. We use array processing techniques—vespagrams, beamforming, and waveform cross correlation—to locate the source of the scattered energy recorded in Southern California. In light of these findings, we conclude with a discussion of the likely sources of lower mantle scattering and of promising future research directions.

2. Methods I: Data Stacking

We obtain a global data set of *PKP* waveforms from an online archive maintained by the Incorporated Research Institutions for Seismology (IRIS). In this study, we use the same data that were used in the single-frequency study by *Mancinelli and Shearer* [2013], composed of ∼150,000 broadband vertical channels (BHZ) recorded from 1990 to 2012 for shallow events (depth < 50 km) with $M_w \geq 5.7$ and deep events with $M_w \geq 5.5$.

At each frequency, we characterize the time and range dependence of the scattered energy by employing an envelope stacking procedure similar to previous *PKP* precursor studies [*Hedlin et al.*, 1997; *Margerin and Nolet*, 2003a; *Mancinelli and Shearer*, 2013]. To characterize the frequency dependence, we repeat the stacking procedure with different bandpass filters (0.4–0.75 Hz, 0.75–1.5 Hz, 1.5–3 Hz, and 3–6 Hz). A separate culling step is applied for each frequency, so each stack may be composed of a different subset of seismograms. The number of seismograms in each stack varies with both range and frequency; the exact numbers are shown in Figure 1. Despite the relatively small number of seismograms in the 3 to 6 Hz stack, bootstrap resampling tests suggest that the stacked precursor amplitudes are stable. We apply this procedure on waveforms filtered from 5 to 10 Hz (not shown), but no signal is discernible at these high frequencies. We also obtain stacks at lower frequencies (0.1–0.2 Hz and 0.2–0.4 Hz, not shown), but these observations may be influenced by diffraction near the *b*-caustic and we do not attempt to model them in this study. At frequencies lower than 0.1 Hz, the precursors are indiscernible because they overlap with the main phase [cf. *Thomas et al.*, 2009].

The most remarkable feature of these stacks is that, with increasing frequency, the precursors become more visible at shorter ranges. Since precursors are understood to be waves scattered into and out of the *b*-caustic at 145° [*Cleary and Haddon*, 1972], this suggests that increased amounts of large-angle scattering is involved at higher frequencies. For 3-D heterogeneity spectra of the form $P(m) \propto m^n$, the scattering pattern is

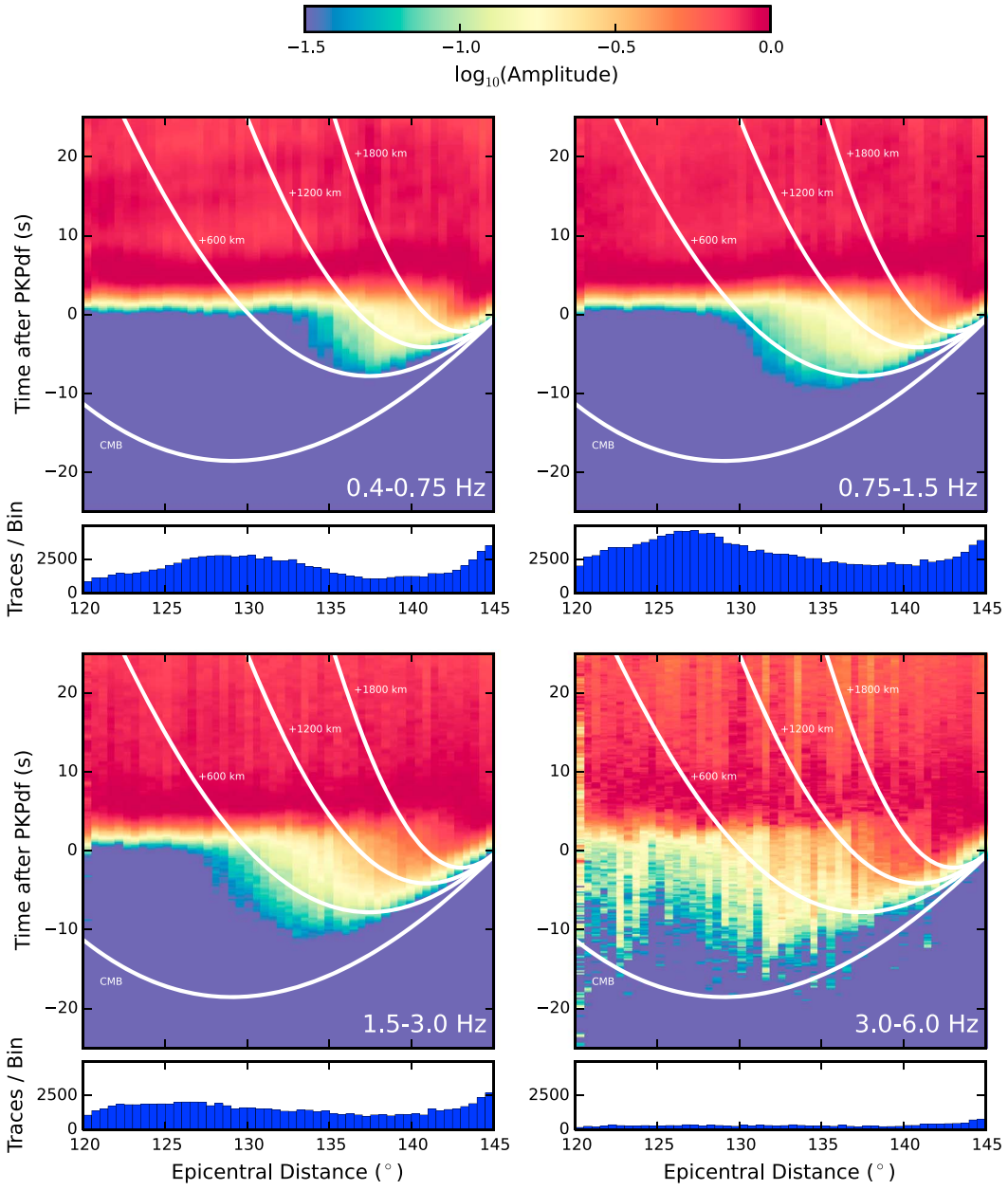

Figure 1. *PKP* precursor stacks, showing globally averaged amplitude as a function of time and epicentral distance for different frequency bands. White curves delineate onset times for scattered energy at various depths in the lower mantle. Histograms show how many seismograms were used in each range bin. See *Mancinelli and Shearer* [2013] for more details.

proportional to m^{4+n} [*Shearer and Earle*, 2004, equation (4)]. Thus, to have increasing scattering power with frequency for a given angle, the power law exponent n must be greater than −4. (For reference, an exponential model has an exponent of −4 in the large wave number limit.) In the following section we will explicitly define various forms of the heterogeneity spectrum and discuss how well each fits the observed *PKP* precursor amplitudes.

3. Methods II: Waveform Modeling

3.1. Random Media Models

To forward model the global stacks, we take a statistical approach. We define heterogeneity power as a function of wave number, and from this assumption we calculate the scattering properties of the medium as

a whole. Each random medium is parameterized by an autocorrelation function, $R(\mathbf{x})$, or, alternatively, its three-dimensional (3-D) Fourier transform, the power spectral density function (PSDF):

$$P(\mathbf{m}) = \iiint_{-\infty}^{\infty} R(\mathbf{x}) e^{-i\mathbf{m}\cdot\mathbf{x}} d\mathbf{x}\,, \tag{1}$$

where $\mathbf{x}$ is the lag position vector and $\mathbf{m}$ is the angular wave number vector. In this study, we consider only random media with isotropic heterogeneity properties. In mathematical terms, R and P depend only on x and m, respectively, where $x = ||\mathbf{x}||$ and $m = ||\mathbf{m}||$ [*Sato et al.*, 2012].

3.2. Phonon Models

Once a PSDF has been defined for each scattering layer within our model, we use a particle-based phonon approach [*Shearer and Earle*, 2004] to forward calculate the wavefield. We run each simulation at a single frequency, f_0, computed as the harmonic mean of the filter bandlimits, f_1 and f_2, i.e.,

$$f_0 = \left[\frac{1}{2}\left(f_1^{-1} + f_2^{-1}\right)\right]^{-1}. \tag{2}$$

This parameter affects the scattering coefficients and intrinsic attenuation.

In this study, we distribute heterogeneity throughout the lowermost 1200 km of the mantle. Previous work has shown that full mantle scattering gives better fits to the time dependence of the 1 Hz stacked precursors than do models where heterogeneity is restricted to the CMB or the D″ region [*Hedlin et al.*, 1997; *Cormier*, 1999; *Margerin and Nolet*, 2003a; *Mancinelli and Shearer*, 2013]. We confirm that a 1200 km thick scattering layer is an appropriate assumption for this work by forward modeling the time dependence at various frequencies. Layers thicker than 1200 km do not appear to affect the synthetics, probably because most of the scattered energy from shallower depths arrives after PKP_{df}. Shrinking the layer down to a thickness of 200 km (i.e., D″ scattering) produces synthetics with constant amplitudes at greater times; this does not match the observed ramp-like time dependence. There is an exception at 4 Hz where the uncertainties in the data stacks are too large to distinguish between the two cases.

Scattering by strong heterogeneity in the lithosphere and upper mantle affects the precursor amplitudes indirectly by broadening the PKP_{df} arrival and exciting postcursors [*Cormier*, 1995; *Thomas et al.*, 2000]. Since the precursors are already spread out in time, the relative amplitude of the precursor wave train is effectively increased. At the cost of computational speed, lithospheric scattering can be modeled directly by the phonon code. Alternatively, one can convolve the output of the phonon code, in power, with an empirical broadening function to account for this effect. Since both methods produce similar results [*Mancinelli and Shearer*, 2013], we use the convolution approach for the sake of computational efficiency.

To be consistent with previous studies, we assume that the P wave quality factor (Q_α) for the inner core is 380 [*Bhattacharyya et al.*, 1993]. This parameter affects the amplitude of the reference phase, PKP_{df}, by which the precursor amplitudes are normalized. All of the examples in the paper assume that this value is constant with frequency. Dispersion measurements of PKP_{df}, however, suggest that Q_α may vary strongly with frequency in the inner core, though it is unclear whether it is increasing or decreasing [*Li and Cormier*, 2002]. To address this issue, we test how the frequency dependence of our synthetics is affected under the assumption that our observations lie on either edge of an absorption band model, i.e., $Q(f) \propto f$ or $Q(f) \propto -f$. These cases represent two extreme scenarios of frequency-dependent inner-core attenuation and should place conservative bounds on our results. The assumed mantle attenuation structure is unlikely to impact our results significantly, as both the precursors and the reference phase take similar paths through the mantle.

Another parameter that we have to set is the velocity-density scaling ratio ν; we choose 0.8 which is the estimated lithospheric value from Birch's law. It has been shown previously that adjusting this parameter has no significant effect on the modeled precursor amplitudes since forward (rather than backward) scattering is involved [*Mancinelli and Shearer*, 2013].

4. Fitting the Frequency Dependence

Before moving into a quantitative discussion of the various models and their data fits, we would like to illustrate how simple models can produce the observed change in the *PKP* precursor range dependence as a

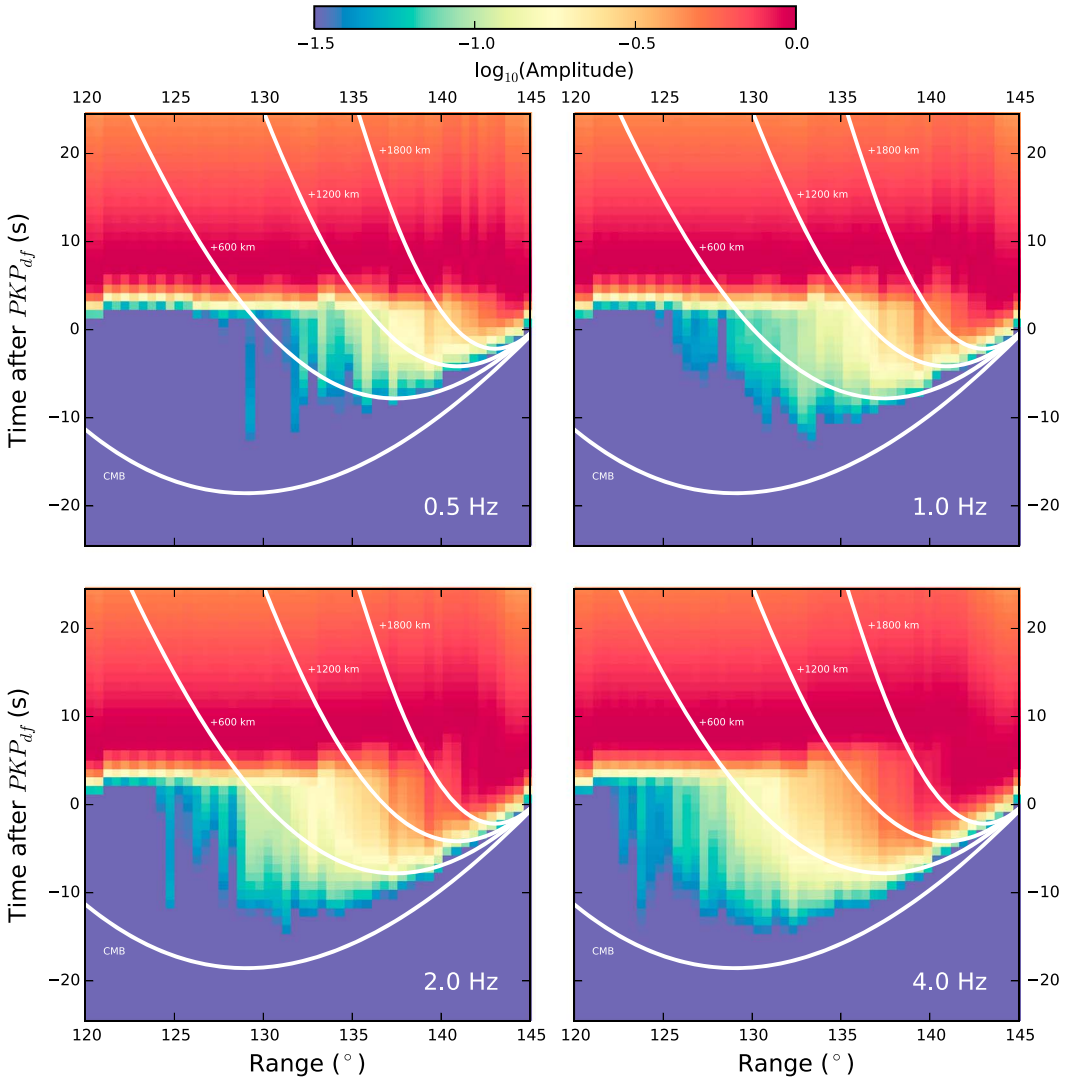

Figure 2. Synthetic *PKP* precursor amplitudes, as computed using the phonon algorithm for H-G random media with $\epsilon = 0.5\%$ and $a = 1000$ km.

function of frequency. Figure 2, for example, shows the phonon code prediction for a random media model with an H-G spectrum (equation (4), below) that contains self-similar heterogeneity at length scales smaller than 1000 km. These images show greater amounts of scattered energy at short ranges with increasing frequency, just as is observed in the data stacks.

For a more quantitative treatment, we compare our global stacks with phonon code predictions of the scattered wavefield assuming various types of random media. We focus on finding a single spectrum that simultaneously fits the range dependence in each of the four frequency bands (0.5, 1, 2, and 4 Hz). To assess the performance of each model, we plot the mean amplitude in a 6 s time window before the onset of PKP_{df} for each range bin. The 95% confidence intervals are estimated using a similar procedure. We find models that achieve reasonable fits to the data by trial and error; a formal inversion is currently impractical due to the time required to run each phonon model and the lack of a convergence criterion that is reliable for a large set of models.

The first spectrum we test is the exponential random media model previously published by *Mancinelli and Shearer* [2013]. The 3-D PSDF is given by

$$P(m) = \frac{8\pi\epsilon^2 a^3}{(1 + a^2 m^2)^2} \tag{3}$$

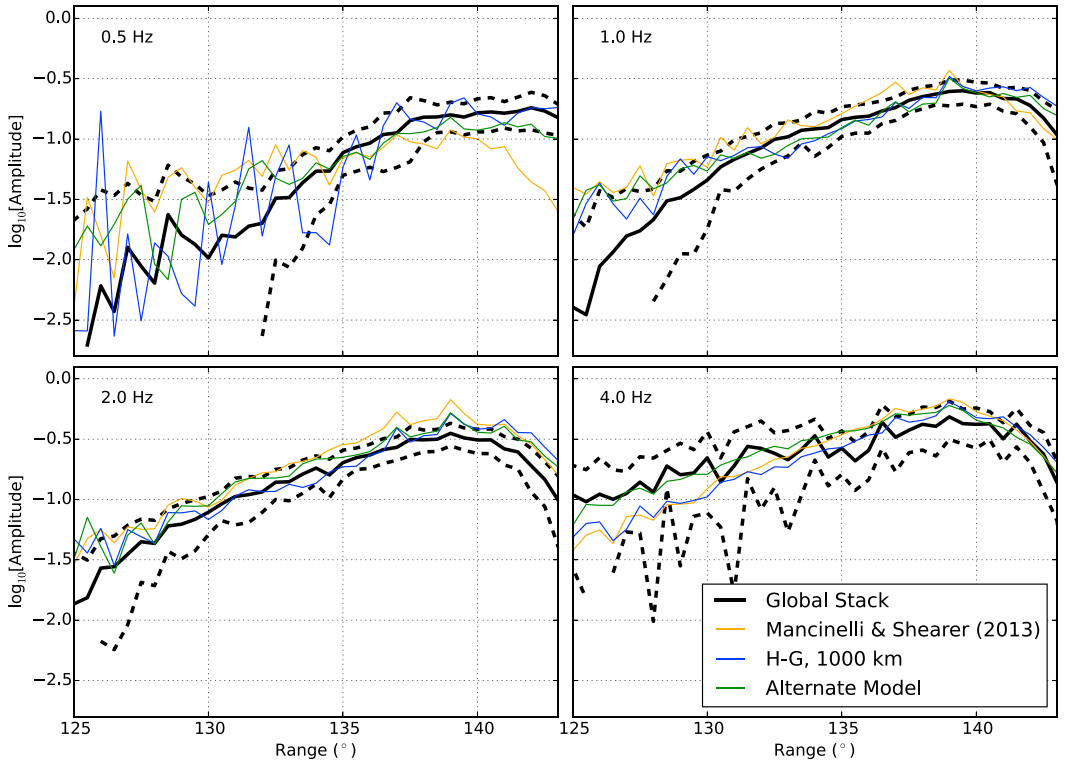

Figure 3. Comparison between observed (thick black curves) and predicted *PKP* precursor amplitudes for three different types of random media. The dashed black lines mark the 95% confidence intervals for the data stacks.

and is plotted in Figure 4 with a correlation length, a, of 6 km and an RMS velocity fluctuation, ϵ, of 0.2%. Exponential models have more small-scale structure than Gaussian models, but most of the variance remains at wavelengths comparable to the correlation length. For a correlation length of about 6 km, as was preferred by *Mancinelli and Shearer* [2013], the observations are fit reasonably well, although there is not enough scattered energy at ranges greater than 138° at 0.5 Hz (Figure 5). If one raises the correlation length of the exponential model to 50 km in order to increase the amount of low-angle scattering, the fits at 1, 2, and 4 Hz degrade because of the relatively rapid falloff rate of the PSDF. Note that the fluctuations in the synthetic amplitude curves at short ranges for 0.5 Hz are not physical. When scattering is very weak, the discrete nature of the phonon method becomes apparent, as only a small number of phonons are scattered to these range bins.

Margerin and Nolet [2003a] proposed an H-G spectrum [after *Henyey and Greenstein*, 1941] that is richer in fine-scale heterogeneity:

$$P(m) = \frac{\epsilon^2 a^3}{(1 + a^2 m^2)^{1.5}}. \tag{4}$$

This spectrum has the property of self-similarity (i.e., constant power per octave) in the limit where $am \gg 1$. When testing these models, we find that an upper limit on the correlation length a is unresolvable, which was also noted by *Margerin and Nolet* [2003a]. As shown in Figure 3, including heterogeneity as large as 30–80 km produces better fits to the long-range (> 140°) precursors at 0.5 Hz. The correlation length of 30 km provides enough large-scale heterogeneity to fit the observations within error, but extending this value to 80 km does produce a model that more closely tracks the 0.5 Hz stack. Increasing the correlation length to values greater than 80 km does not significantly alter the model prediction. We notice that the H-G models systematically overpredict scattering at 2 Hz at ranges greater than 140°.

To address this, we try an alternate model (hereafter referred to by AM) that is even richer than H-G in fine-scale structure:

$$P(m) = \frac{\epsilon^2 a^3}{(1 + a^2 m^2)^{1.3}}. \tag{5}$$

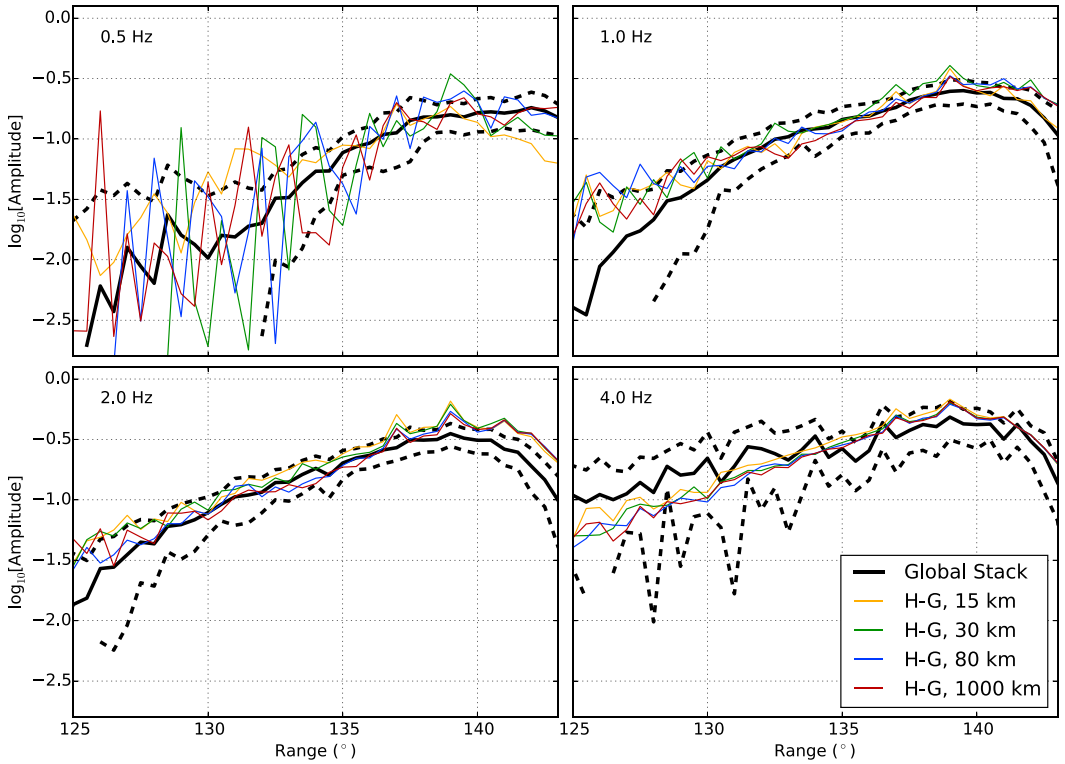

Figure 4. Comparison between observed (thick black curves) and predicted *PKP* precursor amplitudes for a variety of H-G models. The dashed black lines mark the 95% confidence intervals for the data stacks.

This model still fits the range dependence at 0.5, 1, 2, and 4 Hz within the estimated data uncertainties and more closely matches the long-range amplitudes at 2 Hz. Thus, we argue that the AM spectrum has the "best fitting" power law exponent of −2.6. The predictions of the three types of models (i.e., exponential, H-G, and AM) are shown together with the data in Figure 5.

Frequency dependence in inner-core Q_α would have a minor, but noteworthy, effect on our preferred heterogeneity spectrum. Our preferred power law exponent of −2.6 is for frequency-independent Q_α. If Q_α increases linearly with frequency in the inner core, the preferred power law exponent increases to −2.4. In the other extreme case where Q_α goes as 1/frequency, the preferred power law exponent decreases to −2.8.

Although the phonon code accounts for multiple scattering, it is interesting to reevaluate whether single (Born) scattering is a suitable assumption for this problem. For the best fitting H-G model with $a = 80$ km, the lower mantle mean-free paths are 40,000, 14,000, 5900, and 2800 km for 0.5, 1, 2, and 4 Hz, respectively. Benchmarking tests from *Margerin and Nolet* [2003b] suggest that mean-free-times less than 400 s (i.e., mean-free paths shorter than ~5300 km) require multiple scattering to be accurate within 20% error. Therefore, single scattering seems to be adequate for *PKP* precursors at 0.5, 1, and 2 Hz but probably not at 4 Hz. The transport mean-free paths [cf. *Przybilla et al.*, 2009] — 580,000, 290,000, 140,000, and 71,000 km — are considerably larger than the standard mean-free paths. This suggests that the scattering pattern is strongly anisotropic (i.e., most scattering events redirect energy by only a very small angle); this is not surprising considering that the preferred H-G model has increased amounts of large-scale structure. The flattening of the amplitude versus range curve from 2 to 4 Hz (Figures 5 and 3) can be explained by multiple scattering, which tends to smear out the range distribution of energy, resulting in a scattering pattern that appears more isotropic at 4 Hz. We confirm this interpretation by comparing our results with synthetics computed from single scattering only.

In equations (4) and (5), the parameter ϵ represents a scaling factor rather than the RMS velocity fluctuations of the medium. Strictly speaking, the H-G and AM spectra have infinite variance when integrated over the entire spectrum. This, of course, is unphysical. To estimate the physical variance, one should integrate the spectrum only to a wave number corresponding to half of the seismic wavelength [*Margerin and Nolet*, 2003a,

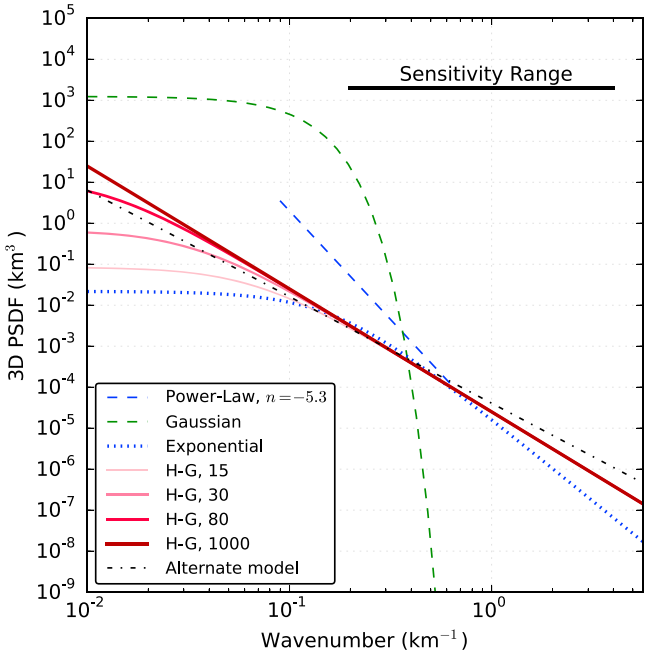

Figure 5. Comparison of heterogeneity spectra proposed to model *PKP* precursors. The blue dotted line is the exponential model published by *Mancinelli and Shearer* [2013]. The dashed curves indicate results from older studies based on more band-limited observations [*Bataille and Flatté*, 1988; *Cormier*, 1995]. The solid colored lines are H-G models with varying correlation lengths (15, 30, 80, and 1000 km) and $\epsilon = 0.5\%$. The dash-dotted line is our Alternate Model (AM) with $a = 1000$ km and $\epsilon = 0.16\%$.

equation (12)]. At lower mantle velocities and at a maximum frequency of 4 Hz, the largest wave number (smallest wavelength, respectively) that we can expect to constrain is ~4 km^{-1} (2 km).

In Figures 5 and 3, a dip in the amplitude curve is visible at long ranges near the *b*-caustic. This dip results from the 6 s averaging window that we use to extract the average precursor amplitude at each range. Although the precursors generally become more energetic at greater ranges, their onset is increasingly delayed approaching 145°.

5. Lateral Variations

Mapping lateral variations in scattering strength may help in understanding the nature of the lower mantle scatterers. This problem is complicated by the fact that both source- and receiver-side heterogeneity scatter precursor energy, and one cannot uniquely map amplitudes observed at a single station to a point of origin in the lower mantle. In an initial attempt at this problem, *Hedlin and Shearer* [2000] inverted for scattering source regions using Global Seismographic Network recordings of *PKP* precursors. The authors noted rough correlations between large-scale tomography anomalies including the African plume and the Tethys trench, but acknowledged that these were "tentative rather than definitive" based on bootstrap resampling tests. In a recent global study of *PKP* precursors, *Waszek et al.* [2015] found no correlation between scattering and large-scale velocity structure at the core-mantle boundary (CMB) and noted much variability of the amplitudes within each region.

Here we attempt to solve the problem in a different way. For each seismogram in our data set, we calculate the CMB piercing points for the PKP_{df} phase. We divide the surface of the CMB into 20° regional cells and group the waveforms by the source-side piercing point. We further divide each regional cell into eight azimuth bins and construct a 2-D stack (e.g., Figure 1) for the data (bandpass filtered from 0.7 to 2.5 Hz) in each bin. For each regional stack, we measure the fractional amplitude deviation in each range bin relative to the global average [*Mancinelli and Shearer*, 2013] for a 20 s window before the onset of PKP_{df}. The mean of the fractional amplitude deviations from all of the range bins gives a single scalar measurement that can be plotted on a map. We quantify the statistical significance of each measurement by bootstrap resampling the set of seismograms and recomputing the 2-D stack and its associated scalar statistic. We deem a regional deviation to

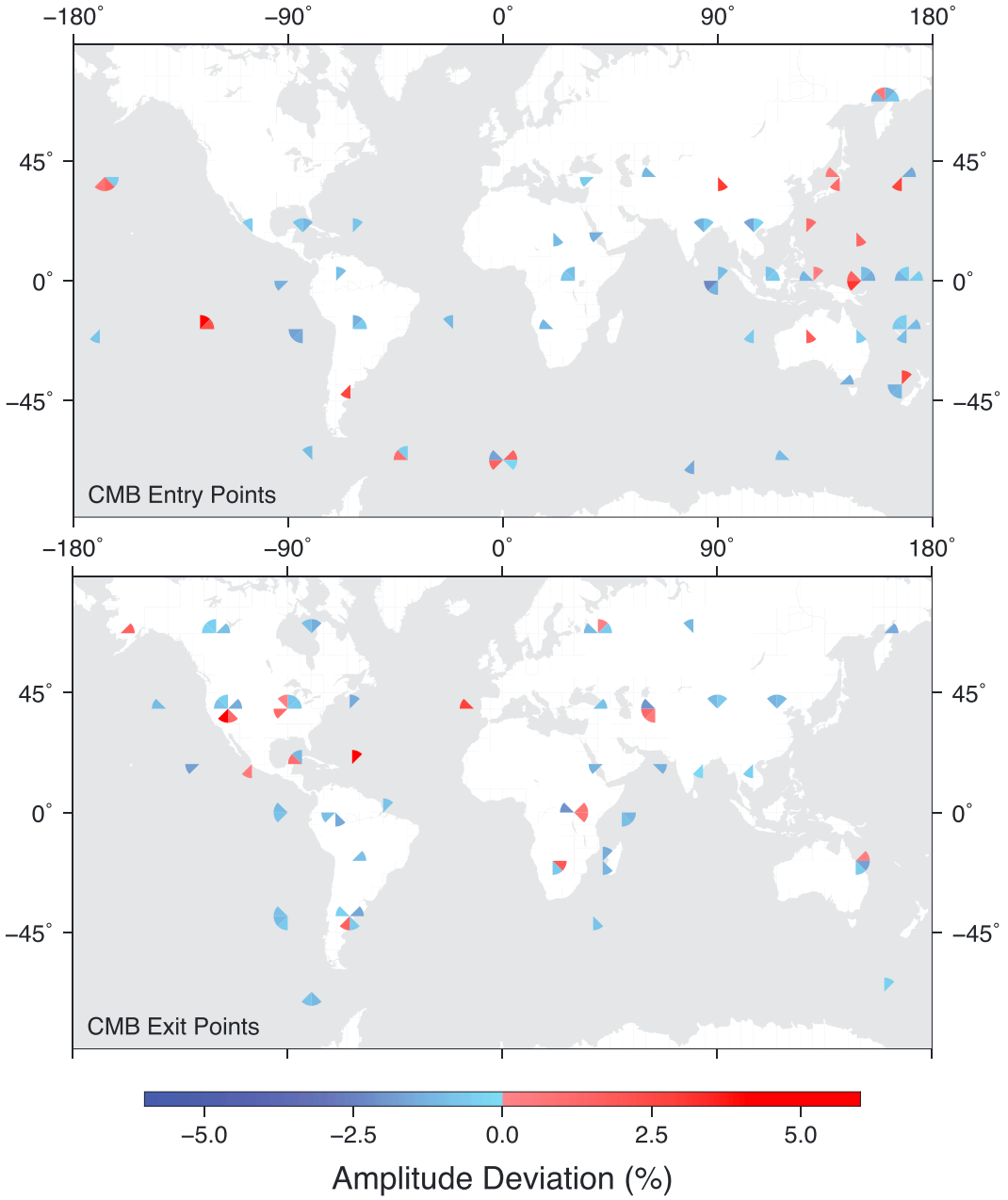

Figure 6. Apparent lateral variations in *PKP* precursor amplitude. Measurements are grouped into 20° cells based on the CMB entry (top map) or CMB exit (bottom map) points for PKP_{df}. Each cell is subdivided into eight azimuth bins, which are plotted as colored pie wedges. The point of each wedge faces the source region (top map) or the receiver region (bottom map). For the top map, of the 118 bins containing 5 or more traces, 74 (63%) deviate significantly (see main text) from the global average. For the bottom map, of the 122 bins containing 5 or more traces, 79 (65%) deviate significantly from the global average. For clarity, only bins with significant deviations are plotted on these maps.

be significantly strong (or weak, respectively) if 95% of 1000 bootstrap estimates are above (or below) 0. We repeat this entire exercise assuming that the scattering occurs near the receiver-side piercing point.

After plotting the median deviations for each bin on the maps in Figure 6, we find large regions of spatially coherent strong scattering beneath the West Pacific, Central/North America, and—to a lesser extent—East Africa. We also identify several regions that display azimuthally dependent scattering behavior. Receiver-side scattering in western North America, for example, shows stronger-than-average amplitudes for rays coming from the south and weaker-than-average amplitudes for rays coming from the north. Also, the region near

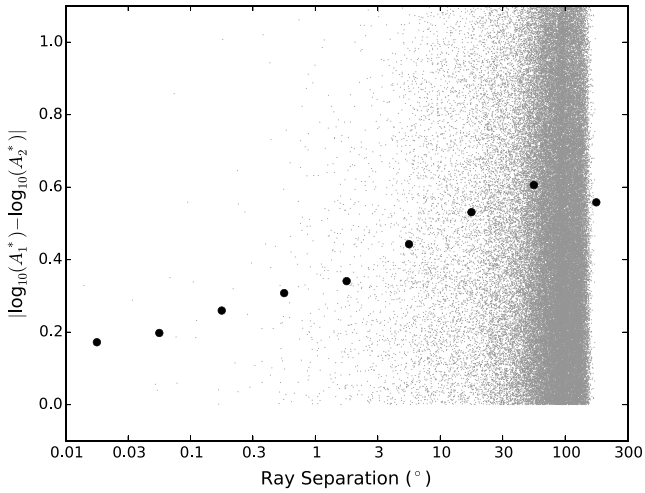

Figure 7. A scatterplot of absolute difference in log amplitude versus ray separation (gray dots). Due to the large number of points, we only plot every 500th one. The median for the complete set of points is plotted in each bin (black circles). We have restricted this analysis to 1 Hz seismograms recorded at ranges from 120 to 140°.

0°E, 60°S displays strong scattering for rays along the ENE-SWS axis and weak scattering for rays along the WNW-ESE axis. These patterns may arise from the shape of the scatterers (i.e., anisotropic heterogeneity) or from differences in scattering properties in the farside scattering regions. In 9 out of the 10 cases where both maps show a deviation in the same bin, both maps agree on the sign of the deviation. The only exception is a bin near 20°N, 70°W.

As an additional check on the reliability of these observations, we conduct a test to determine the average spatial coherence of *PKP* precursor amplitudes for our global data set. What we want is a measure, as a function of ray separation, of how likely it is for two measurements of precursor amplitudes to be similar. We define the log amplitude difference between a pair of precursor waveforms with amplitudes A_1 and A_2 as $\log_{10}(A_1^*) - \log_{10}(A_2^*)$; the asterisks denote that the raw amplitudes have been divided by the global average to correct for systematic variations caused by the range dependence of this phase. The ray separation is defined as $\sqrt{\left(\Delta_s^2 + \Delta_r^2\right)/2}$ where Δ_s and Δ_r are the great circle distances between the two sources and the two receivers, respectively. For each pair, we plot the absolute difference between the log amplitudes versus ray separation in Figure 7. Due to the variability in these measurements, it is difficult to see a trend when looking at the raw scatterplot. To address this, we split the measurements into bins by ray separation (log scale) and plot the median absolute log amplitude difference in each bin (black circles, Figure 7). These medians reveal a trend whereby the absolute differences in log amplitude increase with greater values of ray separation from about 0.02° to 90°. This suggests that large-scale global variations in precursor amplitude do exist within our data set.

Ideally, we would expect the log amplitude difference to approach 0 at increasingly small values of ray separation. We observe, however, that this parameter stops decreasing at ray separations between 0.01° and 0.05°; this is possibly due to incoherent noise recorded at nearby (but not colocated) stations. Independent of the noise, this observation is compatible with a scattering interpretation, as the intensity of the precursors is expected to be exponentially distributed under the assumption that the scattered wavefield is a superposition of many waves with random phases [*Margerin and Nolet*, 2003a, equation (8)]. For the case of colocated channels (not plotted because of log *x* axis), the log amplitude difference is nearly 0.

6. Array Processing

Array methods provide another means to better understand the origin of lower mantle scattering. Determining the slowness and back azimuth of precursor waves can in principle resolve the source-receiver ambiguity discussed in the previous section [*Thomas et al.*, 1999; *Cao and Romanowicz*, 2007; *Frost et al.*, 2013]. In recent years, many broadband stations have been deployed to address questions about the lithosphere and upper mantle. Here we explore how data from these stations could be used to expand global coverage of precursor slowness and back azimuth measurements.

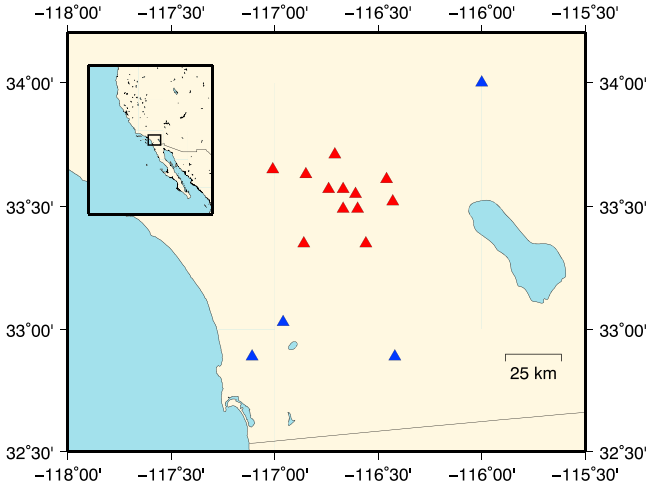

Figure 8. Stations used to locate the origin of *PKP* precursor energy from the M_w 7.6 event on 30 September 2009 in southern Sumatra. Red triangles (Anza Network: BZN, CRY, FRD, KNW, LVA2, PFO, RDM, SND, TRO, WMC; Southern California Seismic Network: DGR, PLM) were used in the beamforming exercise. The blue triangles (Anza Network: HWP, MONP2; Southern California Seismic Network: BEL; Transportable Array: 109C) were added for the cross-correlation analysis.

We apply array processing techniques [*Rost and Thomas*, 2002] to *PKP* precursors from the 30 September 2009 M_w 7.6 earthquake in southern Sumatra recorded by an array of stations in Southern California. The array geometry is shown in Figure 8. The primary goal of this exercise is to determine whether the precursor energy originates from the source- or receiver-side. Using the Seismic Handler analysis program [*Stammler*, 1993], we construct fourth-root vespagrams to constrain the precursor slowness. Prior to stacking, the seismograms are filtered to high frequency (1 – 2 Hz). We find that the precursor energy is diffuse in the vespagrams when assuming the theoretical back azimuth of 305°, yet the energy of the main phase is strong and the slowness is well constrained. As shown in Figure 9, reducing the back azimuth to about 275° gives clear precursor energy in

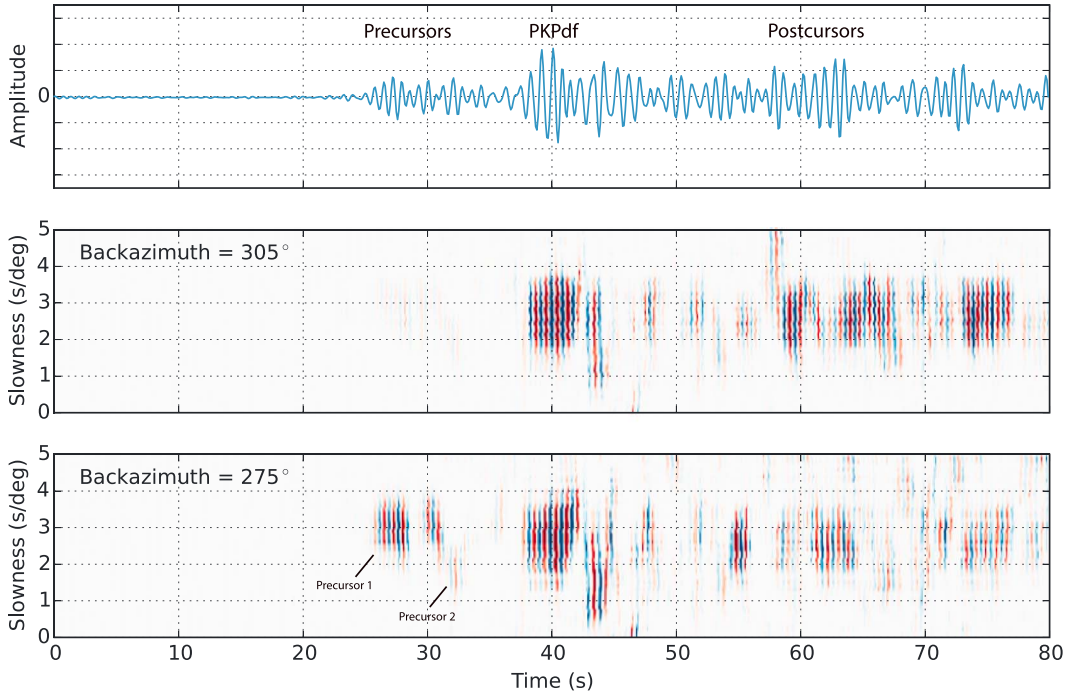

Figure 9. (top) Example seismogram recorded at station PFO filtered from 1 to 2 Hz. (middle) Fourth-root vespagram assuming the theoretical back azimuth of 305° of the recording at the array in Figure 8. (bottom) Same as Figure 9 (middle) but assuming a back azimuth of 275°.

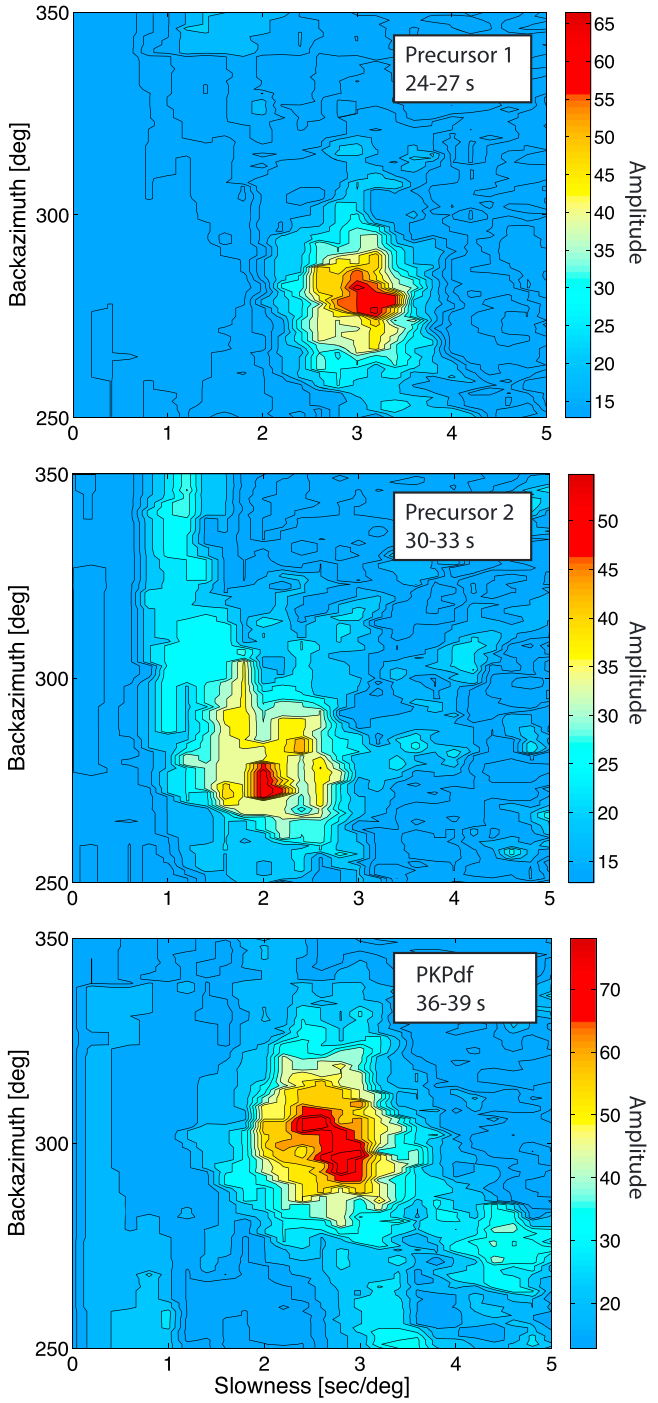

Figure 10. Fourth-root stacks in slowness azimuth space for 3 s windows around (top) the earliest precursor, (middle) the second precursor, and (bottom) the PKP_{df} arrival.

the vespagram with a slowness of 3.2 ± 0.3 s/° followed by a weaker precursor with a slowness of 2.0 ± 0.2 s/°. A grid search over the slowness and back azimuths suggests that the back azimuth of the scattered precursors is 275 ± 7° (Figure 10).

To check the calibration of our array, we measure the back azimuth and slowness of the PKP_{df} phase. We observe the slowness to be 2.6 ± 0.3 s/°. This is significantly larger (by about 0.7 s/°) than the theoretical slowness of 1.9 s/°, suggesting that local structure (e.g., dipping sediment layers) may be biasing our precursor

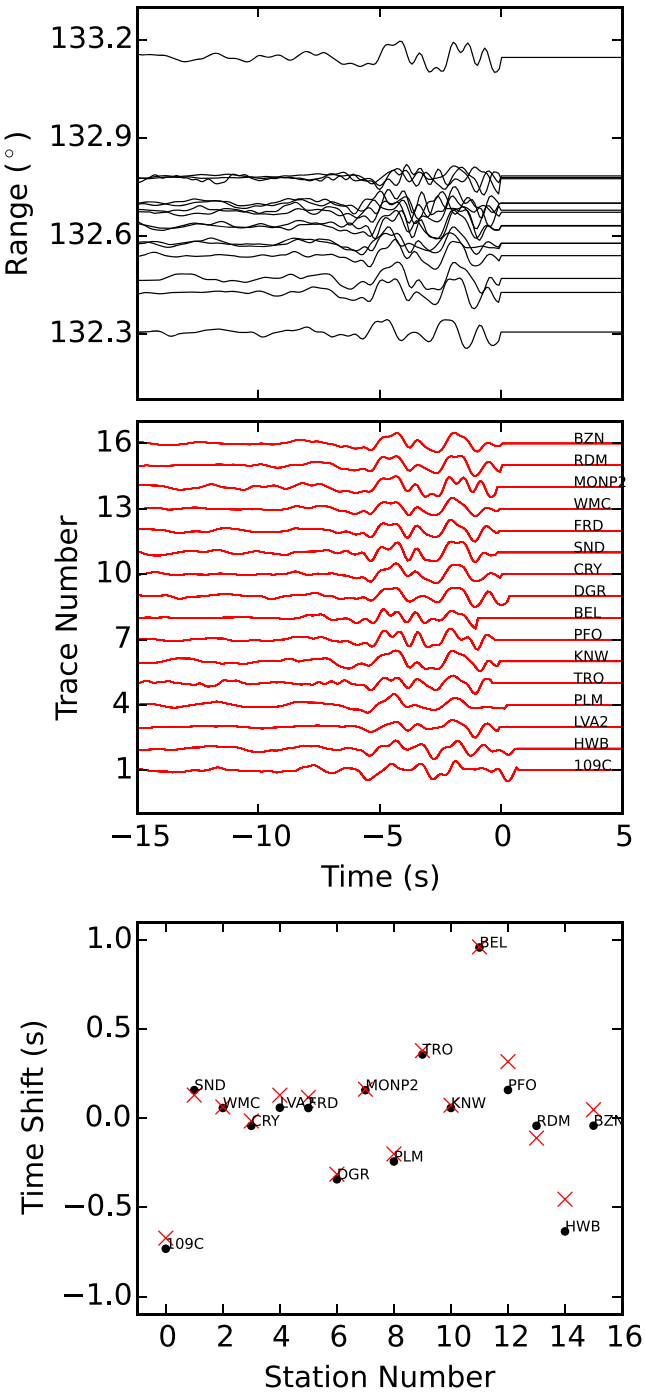

Figure 11. (top) A record section of the *PKP* precursor waveforms filtered from 0.25 to 2.0 Hz. These have been aligned on the reference phase PKP_{df} which was subsequently removed. (middle) Waveform alignment after the cross-correlation algorithm is applied. (bottom) Observed traveltime shifts (black dots) compared with those predicted by a plane wave with slowness 1.4 s/° and a back azimuth of 260° (red crosses). Note that the waveforms were aligned on PKP_{df} prior to cross correlation, so the PKP_{df} slowness (1.9 s/°) should be added to obtain an absolute slowness estimate.

measurements toward larger slownesses. The observed back azimuth of PKP_{df} is 300 ± 10°, which is in agreement with the theoretical back azimuth of 305°. Measuring the slowness of the later arriving phases *PP* (observed: 6.6 ± 0.2 s/°, theoretical: 6.4 s/°) and *SKS* (observed: 4.0 ± 0.2 s/°, theoretical: 2.7 s/°) confirms that our array likely biases the slowness of the precursors. Since the PKP_{df} phase has the closest theoretical slowness to that of the precursors, we apply a correction of −0.5 s/° to the measurements in the previous paragraph.

Developing an ideal set of mislocation vectors for this array would require analyses of many phases from earthquakes all over the globe [e.g., *Krüger and Weber*, 1992], which is beyond the scope of this study. Despite the lack of a detailed mislocation vector, we argue that enough information is present to resolve the source-receiver ambiguity. The measured (and corrected) back azimuths and slownesses suggest that both precursors are scattered from out-of-plane heterogeneity on the receiver side. Synthetic tests with the phonon code confirm this. In addition to the back azimuth and slowness, the arrival time provides information that helps locate the depth of the scatterer. According to ray theoretical calculations, in-plane CMB scattering produces energy that arrives 18 s prior to PKP_{df}; scattering at 600 km above the CMB produces energy 5 s prior to PKP_{df}. The precursors revealed by the vespagram analysis show arrival times 12 and 6 s before PKP_{df}, suggesting that the observed energy is scattered within the deepest 600 km of the mantle. The upper limit of 600 km is a conservative bound because the scattered energy comes from out of plane and thus travels a greater distance. Locations and depth constraints that are more precise may be obtained by using weighted stacking methods [e.g., the *F* statistic, *Frost et al.*, 2013], but even with our relatively simple analysis we are able to resolve the source-receiver ambiguity and determine that the scattered energy comes from outside the great circle path.

We also experiment with another method that relies upon the cross correlation of waveforms to obtain time shifts (with errors) that provide optimal alignment of the precursor waveforms. After aligning the broadband waveforms on the PKP_{df} phase, we filter the seismograms between 0.25 and 2.0 Hz and set all amplitudes to 0 after the theoretical PKP_{df} onset time. Then, we align the collection of precursors using a cross-correlation algorithm [e.g., *Reif et al.*, 2002]. The results of this procedure are shown in Figure 11. From the resulting set of optimal time shifts, we can estimate the best fitting plane wave that corresponds with the arriving energy. Weighted least squares estimation yields a plane wave with 1.4 s/° and a back azimuth of 260°. Since these waveforms are aligned on PKP_{df} prior to cross correlation, a correction of 1.9 s/° is added to this estimate to obtain the absolute slowness of the precursor energy. These values are in rough agreement with those obtained from the beamforming analysis above, again suggesting that the observed precursor energy comes from out-of-plane receiver-side scattering.

We tried this technique on a variety of arrays, and we found that it works best with a relatively broadband filter (0.25–2.0 Hz) and arrays of closely spaced stations. We found many good precursor recordings by Transportable Array (TA) stations, but in most cases the station spacing was too coarse for our methods to perform very well. The precursor waveforms need to be highly similar in order for the cross-correlation algorithm to work, and this is not the case for many of the arrays we tried. EarthScope Flexible Array stations, although generally more closely spaced than TA stations, displayed dissimilar precursor waveforms from station to station, making it difficult to constrain the origin of the scattered energy. We have not yet tried using data from the Flexible Array experiments deployed in the eastern United States, but these may yield better results given the higher-density spacing and presumably simpler local structure. We leave an exploration of these data for future work.

7. Discussion

7.1. The Nature of Lower Mantle Scatterers

The motivation behind the research presented in this paper is to better understand the nature of small-scale heterogeneity in the lowermost mantle. Results from the frequency dependence, spatial coherence, and array processing suggest that the lower mantle consists of a ubiquitous scattering fabric with localized strong scatterers responsible for generating high-amplitude precursors. Here we discuss the implications of our three main results.

1. We find that H-G random media with correlation lengths of 30 km or larger produce good fits to the global stacks of *PKP* precursors at 0.5, 1, 2, and 4 Hz. Although the H-G model was previously proposed by *Margerin and Nolet* [2003a] to model the range dependence of precursor amplitudes at a single frequency,

their focus was to increase the amount of heterogeneity at length scales smaller than 15 km. They tested H-G models with correlation lengths of 15, 30, and 80 km and concluded that their observations could not favor any of these models over the others. Here we have confirmed that the H-G model outperforms the exponential model, but we argue that correlation lengths $\geq$30 km provide better fits to the 0.5 Hz observations. This represents an improved global constraint from the *Margerin and Nolet* [2003a] study and confirms the larger-scale lower mantle scatterers reported in regional studies of *PKP* precursors [*Wen and Helmberger*, 1998; *Thomas et al.*, 1999].

As things stand, it is likely that the lower mantle heterogeneity obeys either an H-G or AM type spectrum with an arbitrarily large correlation length. In the limit where the correlation length increases to a very large value, the H-G and AM models approach a power law form with exponents −3 and −2.6. The H-G spectrum possesses constant power per octave and has been associated with models of a marble cake mantle structure resulting from convective mixing [*Batchelor*, 1959; *Antonsen and Ott*, 1991; *Agranier et al.*, 2005; *Ricard et al.*, 2014]. At lowermost mantle pressures and temperatures the shear wave velocity contrast between basalt and harzburgite is about 2–4% [*Stixrude and Lithgow-Bertelloni*, 2012]. In the upper mantle, the shear wave velocity contrast can be considerably larger, 10–20% [*Xu et al.*, 2008]. This may explain why globally averaged small-scale velocity perturbations in the upper mantle and lithosphere have been reported to be an order of magnitude larger than those in the lower mantle [*Shearer and Earle*, 2004, 2008]. Another plausible idea is that short-wavelength changes in the fast axis of an anisotropic fabric can scatter energy much like volumetric heterogeneity can. Such textures — either volumetric or anisotropic — may be the source of the ubiquitous *PKP* precursors, which have been observed in almost every region of the globe [*Hedlin and Shearer*, 2000; *Waszek et al.*, 2015].

Of course, this result relies on the assumption that ray theory is valid at 0.5 Hz for ranges as large as 142°. Close to the *b*-caustic (at 145°) the effect of diffraction is expected to become increasingly more important at reduced frequencies. The combined effects of diffraction and scattering are difficult to evaluate at this time because of the great computational cost in running global spectral element simulations accurate to a period of 1 s.

2. We observe significant large-scale lateral variations in *PKP* precursor amplitude. Spatially coherent regions of strong scattering appear beneath the West Pacific, Central/North America, and — to a lesser extent — East Africa. The anomalies beneath Central/North America and the West Pacific were previously noted by *Hedlin and Shearer* [2000], who suggested that the strong scattering may be due to remnants of the Farallon Slab and Tethys Trench. A small area of strong scattering east of Japan is shown by *Hedlin and Shearer* [2000], but we find a much broader region of strong scattering that extends throughout much of the West Pacific. We also observe a few cases of azimuthally dependent scattering [e.g., *Cormier*, 1999]; these may be caused by anisotropic heterogeneity within the observed regions.

   It has been suggested that regional variations in apparent precursor amplitude may be due to lateral differences in inner-core velocity and attenuation structure that affect the amplitude of the reference phase, PKP_{df}. This effect has been shown to be quite large at the hemispherical scale, yielding amplitudes for the Eastern Hemisphere that are, on average, 30% larger than precursor amplitudes in the Western Hemisphere [*Waszek et al.*, 2015]. In principle, our bootstrapping approach avoids mapping such a signal from the inner core, as each regional stack ideally contains measurements from a variety of raypaths that sample different parts of the inner core but the same part of the lower mantle. In practice, however, the global distribution of earthquakes and seismometers is nonuniform, so some regional stacks may be dominated by raypaths that are grouped closely together. In such a scenario, inner-core structure would be more likely to affect our maps. Preliminary tests where we subdivide each regional stack into 1° × 1° subregions, and perform bootstrap resampling analyses on random subsets of these subregions, suggest that this is not a significant issue.
3. We experiment with using various arrays of stations to constrain the slowness and back azimuth of *PKP* precursor energy, as has been done in some previous studies. It is likely that dense local arrays deployed to address near-surface issues may expand our coverage of scattering in the deep Earth. Although mislocation vectors may be lacking for these improvised arrays, in many cases they may be able to resolve the source-receiver ambiguity. We present an example where the array processing techniques succeeded in locating out-of-plane receiver-side scattering close to the CMB near Southern California. The fact that arrays can precisely locate the slowness and back azimuth of precursor arrivals implies that small-scale heterogeneity may be, in many cases, quite localized. If this is the case, however, one might expect some regions to be

devoid of scattering. This has not been routinely observed. Expanding array coverage should help address the question of how much scattered energy comes from localized, rather than distributed, heterogeneity.

7.2. Future Work

Although this work has focused exclusively on *PKP* precursors, other phases may provide additional information about small-scale lower mantle heterogeneity. *Bataille and Lund* [1996] proposed multiple scattering in a low-velocity layer near the CMB to explain the long duration of another scattered phase, P_{diff} coda. The problem with this model, however, is that it fails to match the emergent nature of *PKP* precursors. In an initial attempt to address this issue, the time and range dependence of 1 Hz P_{diff} coda was shown to be consistent with 1% perturbations throughout the lower mantle with a correlation length of 2 km under the assumption of single scattering [*Earle and Shearer*, 2001]. More recent studies have shown that perturbations of this magnitude are too strong [*Mancinelli and Shearer*, 2013], so further research should be done to determine the range of heterogeneity spectra that can match the observed amplitudes of P_{diff} coda, while maintaining reasonable fits to *PKP* precursors.

P_{diff} coda filtered at longer periods could, in principle, help constrain heterogeneity power at intermediate scales of tens to hundreds of meters. This phase is challenging to model with the phonon code because it involves both diffraction and scattering. We performed SPECFEM3D_GLOBE [*Komatitsch and Tromp*, 2002a, 2002b; *Chaljub et al.*, 2007] simulations for 3-D Earth models with random velocity heterogeneity distributed throughout the lower mantle. Preliminary tests, however, suggest that all of the long-period (20–40 s) P_{diff} coda energy can be modeled by reasonable amounts of heterogeneity in the lithosphere and upper mantle, so unique constraints on intermediate-scale heterogeneity in the lower mantle are not likely to come from this phase.

Another scattered phase, $P' \bullet P'$, consists of out-of-plane scattered energy from various depths in the mantle [*Earle et al.*, 2011]. The long time window for this phase suggests that it can be used to characterize heterogeneity throughout the mantle [*Rost et al.*, 2015]. Although some success has resulted from using array techniques on this phase [*Earle et al.*, 2011; *Rost et al.*, 2015], characterizing its globally averaged time, range, and frequency dependence has been challenging thus far due to high-amplitude signal-generated noise from the surface waves that precede this phase. Future studies of $P' \bullet P'$ should focus on using deep earthquakes and innovative stacking methods to isolate the scattered energy associated with $P'P'$.

Acknowledgments

This research was supported by National Science Foundation grant EAR-111111 and the National Science Foundation Graduate Research Fellowship Program. The facilities of IRIS Data Services, and specifically the IRIS Data Management Center (https://ds.iris.edu/ds/nodes/dmc/), were used for access to waveforms and related metadata used in this study. The data set for this paper is available by contacting the corresponding author at njmancin@ucsd.edu. IRIS Data Services are funded through the Seismological Facilities for the Advancement of Geoscience and EarthScope (SAGE) Proposal of the National Science Foundation under Cooperative agreement EAR-1261681. Computing resources for the SPECFEM3D_GLOBE simulations were provided by the Extreme Science and Engineering Discovery Environment (XSEDE), which is supported by National Science Foundation grant ACI-1053575. We are grateful for constructive suggestions from two anonymous reviewers.

References

Agranier, A., J. Blichert-Toft, D. Graham, V. Debaille, P. Schiano, and F. Albarède (2005), The spectra of isotopic heterogeneities along the mid-Atlantic Ridge, *Earth Planet. Sci. Lett.*, *238*, 96–109, doi:10.1016/j.epsl.2005.07.011.

Antonsen, T. M., and E. Ott (1991), Multifractal power spectra of passive scalars convected by chaotic fluid flows, *Phys. Rev. A*, *44*(2), 851–857.

Bataille, K., and S. M. Flatté (1988), Inhomogeneities near the core–mantle boundary inferred from scattered *PKP* waves recorded at the Global Digital Seismograph Network, *J. Geophys. Res.*, *93*(B12), 15,057–15,064, doi:10.1029/JB093iB12p15057.

Bataille, K., and F. Lund (1996), Strong scattering of short-period seismic waves by the core-mantle boundary and the *P*-diffracted wave, *Geophys. Res. Lett.*, *23*(18), 2413–2416, doi:10.1029/96GL02225.

Batchelor, G. K. (1959), Small-scale variation of convected quantities like temperature in turbulent fluid: Part 1. General discussion and the case of small conductivity, *J. Fluid Mech.*, *5*(01), 113–133, doi:10.1017/S002211205900009X.

Bhattacharyya, J., P. Shearer, and G. Masters (1993), Inner core attenuation from short-period *PKP*(BC) versus *PKP*(DF) waveforms, *Geophys. J. Int.*, *114*(1), 1–11, doi:10.1111/j.1365-246X.1993.tb01461.x.

Cao, A., and B. Romanowicz (2007), Locating scatterers in the mantle using array analysis of *PKP* precursors from an earthquake doublet, *Earth Planet. Sci. Lett.*, *255*(1–2), 22–31, doi:10.1016/j.epsl.2006.12.002.

Chaljub, E., D. Komatitsch, J.-P. Vilotte, Y. Capdeville, B. Valette, and G. Festa (2007), Spectral-element analysis in seismology, *Adv. Geophys.*, *48*, 365–419.

Cleary, J. R., and R. A. W. Haddon (1972), Seismic wave scattering near the core-mantle boundary: A new interpretation of precursors to *PKP*, *Nature*, *240*, 549–551, doi:10.1038/240549a0.

Cormier, V. F. (1995), Time-domain modelling of PKIKP precursors for constraints on the heterogeneity in the lowermost mantle, *Geophys. J. Int.*, *121*, 725–736.

Cormier, V. F. (1999), Anisotropy of heterogeneity scale lengths in the lower mantle from PKIKP precursors, *Geophys. J. Int.*, *136*(2), 373–384, doi:10.1046/j.1365-246X.1999.00736.x.

Doornbos, D. J. (1978), On seismic-wave scattering by a rough core–mantle boundary, *Geophys. J. R. Astron. Soc.*, *53*, 643–662.

Earle, P. S., and P. M. Shearer (2001), Distribution of fine-scale mantle heterogeneity from observations of P_{diff} coda, *Bull. Seismol. Soc. Am.*, *91*(6), 1875–1881, doi:10.1785/0120000285.

Earle, P. S., S. Rost, P. M. Shearer, and C. Thomas (2011), Scattered $P'P'$ waves observed at short distances, *Bull. Seismol. Soc. Am.*, *101*(6), 2843–2854, doi:10.1785/0120110157.

Frost, D. A., S. Rost, N. D. Selby, and G. W. Stuart (2013), Detection of a tall ridge at the core–mantle boundary from scattered *PKP* energy, *Geophys. J. Int.*, *195*(1), 558–574, doi:10.1093/gji/ggt242.

Hedlin, M. A. H., and P. M. Shearer (2000), An analysis of large-scale variations in small-scale mantle heterogeneity using Global Seismographic Network recordings of precursors to *PKP*, *J. Geophys. Res.*, *105*(B6), 13,655–13,673.

Hedlin, M. A. H., P. M. Shearer, and P. S. Earle (1997), Seismic evidence for small-scale heterogeneity throughout the Earth's mantle, *Nature*, *387*(6629), 145–150, doi:10.1038/387145a0.

Henyey, L. C., and J. L. Greenstein (1941), Diffuse radiation in the galaxy, *Astrophys. J.*, *93*, 70–83, doi:10.1086/144246.

Komatitsch, D., and J. Tromp (2002a), Spectral-element simulations of global seismic wave propagation—I. Validation, *Geophys. J. Int.*, *149*(2), 390–412, doi:10.1046/j.1365-246X.2002.01653.x.

Komatitsch, D., and J. Tromp (2002b), Spectral-element simulations of global seismic wave propagation—II. Three-dimensional models, oceans, rotation, and self-gravitation, *Geophys. J. Int.*, *149*(2), 390–412, doi:10.1046/j.1365-246X.2002.01653.x.

Krüger, F., and M. Weber (1992), The effect of low-velocity sediments on the mislocation vectors of the GRF array, *Geophys. J. Int.*, *108*, 387–393, doi:10.1111/j.1365-246X.1992.tb00866.x.

Li, X., and V. F. Cormier (2002), Frequency-dependent seismic attenuation in the inner core, 1. A viscoelastic interpretation, *J. Geophys. Res.*, *107*(B12), 2362, doi:10.1029/2002JB001796.

Mancinelli, N. J., and P. M. Shearer (2013), Reconciling discrepancies among estimates of small-scale mantle heterogeneity from *PKP* precursors, *Geophys. J. Int.*, *195*(3), 1721–1729, doi:10.1093/gji/ggt319.

Margerin, L., and G. Nolet (2003a), Multiple scattering of high-frequency seismic waves in the deep Earth: *PKP* precursor analysis and inversion for mantle granularity, *J. Geophys. Res.*, *108*(B11), 2514, doi:10.1029/2003JB002455.

Margerin, L., and G. Nolet (2003b), Multiple scattering of high-frequency seismic waves in the deep Earth: Modeling and numerical examples, *J. Geophys. Res.*, *108*(B5), 2234, doi:10.1029/2002JB001974.

Przybilla, J., U. Wegler, and M. Korn (2009), Estimation of crustal scattering parameters with elastic radiative transfer theory, *Geophys. J. Int.*, *178*(2), 1105–1111, doi:10.1111/j.1365-246X.2009.04204.x.

Reif, C., G. Masters, P. Shearer, and G. Laske (2002), Cluster analysis of long-period waveforms: Implications for global tomography, *Eos Trans. AGU*, *83*(47), 954.

Ricard, Y., S. Durand, J.-P. Montagner, and F. Chambat (2014), Is there seismic attenuation in the mantle?, *Earth Planet. Sci. Lett.*, *388*, 257–264, doi:10.1016/j.epsl.2013.12.008.

Rost, S., and C. Thomas (2002), Array seismology: Methods and applications, *Rev. Geophys.*, *40*(3), 1008, doi:10.1029/2000RG000100.

Rost, S., P. S. Earle, P. M. Shearer, D. A. Frost, and N. D. Selby (2015), Seismic detections of small-scale heterogeneities in the deep Earth, in *The Earth's Mantle Heterogenous Mantle: A Geophysical, Geodynamical, and Geochemical Perspective*, edited by A. Khan and F. Deschamps, pp. 367–390, Springer, New York, doi:10.1007/978-3-319-15627-9.

Sato, H., M. C. Fehler, and T. Maeda (2012), *Seismic Wave Propagation and Scattering in the Heterogeneous Earth*, 2nd ed., Springer, New York.

Shearer, P. M., and P. S. Earle (2004), The global short-period wavefield modelled with a Monte Carlo seismic phonon method, *Geophys. J. Int.*, *158*(3), 1103–1117, doi:10.1111/j.1365-246X.2004.02378.x.

Shearer, P. M., and P. S. Earle (2008), Observing and modeling elastic scattering in the deep Earth, *Adv. Geophys.*, *50*, 167–193.

Stammler, K. (1993), SeismicHandler—Programmable multichannel data handler for interactive and automatic processing of seismological analyses, *Comput. Geosci.*, *19*(2), 135–140, doi:10.1016/0098-3004(93)90110-Q.

Stixrude, L., and C. Lithgow-Bertelloni (2012), Geophysics of chemical heterogeneity in the mantle, *Ann. Rev. Earth Planet. Sci.*, *40*, 569–595, doi:10.1146/annurev.earth.36.031207.124244.

Thomas, C., M. Weber, C. W. Wicks, and F. Scherbaum (1999), Small scatterers in the lower mantle observed at German broadband arrays, *J. Geophys. Res.*, *104*(B7), 15,073–15,088.

Thomas, C., H. Igel, M. Weber, and F. Scherbaum (2000), Acoustic simulation of *P*-wave propagation in a heterogeneous spherical Earth: Numerical method and application to precursor waves to *PKP*df, *Geophys. J. Int.*, *141*, 307–320, doi:10.1046/j.1365-246X.2000.00079.x.

Thomas, C., J. M. Kendall, and G. Helffrich (2009), Probing two low-velocity regions with *PKP b*-caustic amplitudes and scattering, *Geophys. J. Int.*, *178*, 503–512, doi:10.1111/j.1365-246X.2009.04189.x.

Vidale, J. E., and M. A. H. Hedlin (1998), Evidence for partial melt at the core–mantle boundary north of Tonga from the strong scattering of seismic waves, *Nature*, *391*(6668), 682–685.

Waszek, L., C. Thomas, and A. Deuss (2015), *PKP* precursors: Implications for global scatterers, *Geophys. Res. Lett.*, *42*, 3829–3838, doi:10.1002/2015GL063869.

Wen, L., and D. V. Helmberger (1998), Ultra-low velocity zones near the core-mantle boundary from broadband *PKP* precursors, *Science*, *279*(5357), 1701–1703, doi:10.1126/science.279.5357.1701.

Xu, W., C. Lithgow-Bertelloni, L. Stixrude, and J. Ritsema (2008), The effect of bulk composition and temperature on mantle seismic structure, *Earth Planet. Sci. Lett.*, *275*, 70–79, doi:10.1016/j.epsl.2008.08.012.

Yao, J., and L. Wen (2014), Seismic structure and ultra-low velocity zones at the base of the Earth's mantle beneath Southeast Asia, *Phys. Earth Planet. Inter.*, *233*, 103–111, doi:10.1016/j.pepi.2014.05.009.